

Redshifts of Emission Line Objects in the Hubble Ultra Deep Field

Chun Xu^{1,2}, Norbert Pirzkal¹, Sangeeta Malhotra^{1,8}, James E. Rhoads^{1,8}, Bahram Mobasher¹, Emanuele Daddi³, Caryl Gronwall⁴, Nimish P. Hathi⁸, Nino Panagia¹, Henry C. Ferguson¹, Anton M. Koekemoer¹, Martin Kümmel⁵, Leonidas A. Moustakas¹, Anna Pasquali⁶, Sperello di Serego Alighieri⁷, Joel Vernet⁷, Jeremy R. Walsh⁵, Rogier Windhorst⁸, Haojing Yan⁹

ABSTRACT

We present redshifts for 115 emission line objects in the Hubble Ultra Deep Field (UDF) identified through the GRISM ACS Program for Extragalactic Science (GRAPES) project using the slitless grism spectroscopy mode of the ACS Camera on the Hubble Space Telescope (HST). The sample was selected by an emission line search on all extracted 1-dimensional GRAPES spectra. We identify the emission lines using line wavelength ratios where multiple lines are detected in the grism wavelength range ($5800\text{\AA} \lesssim \lambda \lesssim 9600\text{\AA}$), and using photometric redshift information where multiple lines are unavailable. We then derive redshifts using the identified lines. Our redshifts are accurate to $\delta z \approx 0.009$, based on both statistical uncertainty estimates and comparison with published ground-based spectra. Over 40% of our sample is fainter than typical magnitude limits for ground-based spectroscopy (with $i_{AB} > 25$ mag). Such emission lines would

¹Space Telescope Science Institute, 3700 San Martin Drive, Baltimore, MD 21218.

²Email: cxu_25 "at" yahoo.com

³*Spitzer Fellow*, National Optical Astronomy Observatory, P.O. Box 26732, Tucson, AZ 85726.

⁴Department of Astronomy, Pennsylvania State University, University Park, PA 16802.

⁵ESO/ST-ECF, Karl-Schwarzschild-Strasse 2, D-85748, Garching, Germany.

⁶Institute of Astronomy, ETH Hoenggerberg, CH-8093 Zurich, Switzerland.

⁷INAF - Osservatorio Astrofisico di Arcetri, Largo E. Fermi 5, I-50125 Firenze, Italy.

⁸School of Earth and Space Exploration, Arizona State University, Tempe, AZ 85287.

⁹Spitzer Science Center, Caltech, MS 100-22, Pasadena, CA 91125.

likely remain undiscovered without our deep survey. The emission line objects fall into 3 categories: 1) Most are low to moderate redshift galaxies ($0 \leq z \leq 2$), including many actively star forming galaxies with strong HII regions; 2) 9 are high redshift ($4 \leq z \leq 7$) Lyman- α emitters; and 3) at least 3 are candidate AGNs.

Subject headings: galaxies: high redshift — galaxies: formation — galaxies: starburst

1. Introduction

The GRISM ACS Program for Extra-galactic Science (GRAPES) project is a slitless spectroscopic survey of the Hubble Ultra Deep Field (UDF) region (Beckwith 2006). GRAPES exploits the high spatial resolution and low background of the G800L grism on the Advanced Camera for Surveys (ACS). The resulting spectra can detect continuum levels down to $z_{AB} > 27$ magnitude, making them the deepest ever obtained for continuum spectroscopy. Additionally, they can detect emission lines to $\sim 5 \times 10^{-18} \text{ erg cm}^{-2} \text{ s}^{-1}$, more sensitive than any previous slitless survey and comparable to the sensitivities of typical slit spectra on 6–10 meter class telescopes. GRAPES thereby provides a rich data set with a wide range of potential applications, from Lyman breaks in distant galaxies (Malhotra et al. 2005), to 4000 Å breaks in galaxies with older stellar populations (Daddi et al. 2005; Pasquali et al. 2005), to spectral classification of faint Galactic stars (Pirzkal et al. 2005).

The use of slitless spectrographic surveys to search for emission-line galaxies dates back more than three decades. The most famous surveys of this type used objective prisms on Schmidt telescopes. Early surveys utilized photographic plates in order to maximize the field-of-view. Surveys of this type include the Tololo (Smith 1975; Smith et al. 1976) and Michigan (MacAlpine et al. 1977, MacAlpine & Williams 1981) surveys. More recently the Universidad Complutense de Madrid (Zamorano et al. 1994, 1996) survey defined a well-studied sample of H α selected galaxies. The advent of large CCD detectors available on Schmidt telescopes has made possible large-scale digital objective-prism surveys. The first of this type is the KPNO International Spectroscopic Survey (KISS; Salzer et al. 2000). Objective prism surveys from the ground have in general been most effective for relatively nearby galaxies. Efforts to search for high redshift Lyman- α emitting galaxies with slitless spectrographic surveys also be dated back to as early as 1980s (e.g., Koo & Kron 1980; for a review, see Pritchet 1994). However, only the advent of slitless spectroscopic capabilities on the Hubble Space Telescope on both the STIS and NICMOS instruments, enabled such surveys to achieve high sensitivity. Examples include H α from redshift 0.75 to 1.9 with

NICMOS (McCarthy et al. 1999; Yan et al. 1999) and [O II] $\lambda 3727$ from 0.43 to 1.7 with STIS (Teplitz et al. 2003a,b). These surveys were done in parallel observing mode to maximize the total area observed. These were followed by parallel mode surveys using ACS during the first year of ACS operations: The APPLES survey, led by Rhoads (see Pasquali et al 2005), and a similar effort led by L. Yan (see Drozdovsky et al 2005). GRAPES is a natural successor to these efforts, and represents a major step forward in sensitivity and robustness, thanks to the improved experimental design allowed by pointed observations.

In the present paper, we present a redshift catalog for strong emission lines galaxies identified in the GRAPES spectra for both nearby and distant galaxies. We combine our line wavelengths with photometric redshift estimates from broad band photometry to obtain accurate redshifts for most of the emission line sources in the UDF. Such redshifts are a starting point in studies of cosmological evolution. Emission line galaxies are of particular physical interest for several reasons. $H\alpha$, [O II] $\lambda 3727$ and [O III] $\lambda\lambda 4959, 5007$ can be used to study the evolution of star formation rate (e.g., Gallego et al. 1995, 2002). We will present such analysis from the GRAPES emission lines, including the completeness analysis, in forthcoming paper (Gronwall et al., in preparation). $\text{Ly}\alpha$ can be a prominent signpost of actively star forming galaxies at the highest presently available redshifts, and can be used to probe physical conditions in these galaxies (Malhotra & Rhoads 2002) and to study the ionization state of the intergalactic medium (Malhotra & Rhoads 2004, 2006).

The paper is organized as follows. We describe the data reduction and emission line search procedure in section 2, then we present our results in section 3, followed by a discussion section (section 4). We present our redshift catalog for emission line galaxies in table 1.

2. Observations and Reductions

Slitless spectroscopy using the ACS G800L grism on the Hubble Space Telescope has its own unique characteristics, which we discuss briefly here as useful background to understanding the strengths and limitations of our data set. First, the high spatial resolution and low sky background afforded by HST result in highly sensitive spectra. Second, the dispersion is low, at 40\AA per pixel. Third, the slitless nature of the observations imply that spectra may overlap, and that the effective spectral resolution scales inversely with the angular size of the source. Thus, to detect an emission line, its equivalent width (in \AA) should not be far below the object size times spectrograph dispersion. Our selection effects for a range of continuum magnitude, line flux, and equivalent width are discussed below. Fourth, continuum subtraction is nontrivial in grism spectra. The basic difficulty is in identifying object-free regions of the dispersed grism data to scale and subtract a sky model. This can be done

very well, but not perfectly, with residuals at the level of a few $\times 10^{-4}$ counts/s/pixel, corresponding to $\sim 10^{-3}$ of the sky count rate (see Pirzkal et al 2004 for further discussion). The implication for emission line studies is that equivalent width measurements at the faintest continuum fluxes are subject to potential error induced by continuum subtraction residuals. Fifth, the grism signal-to-noise ratio and the contamination can both be helped by using a narrow extraction window, but this comes at the cost of aperture losses in the extracted spectrum. Because the ACS point spread function does not vary strongly with wavelength, the aperture losses should be largely wavelength independent, and will have little effect on line ratio measurements.

The GRAPES observations consisted of a total of 5 epochs of observations with comparable exposure time at 5 different orientations (also quoted as Position Angles or PAs). By splitting the observations into different orientations, we are able to mitigate the effects of overlapping spectra: most objects are uncontaminated in at least some roll angles. Due to slight offsets in sky coverage for different roll angles, we have varied depth in the exposures. About 10.5 square arcmin are covered by at least 4 roll angles, and more than 12.5 square arcmin are covered by at least one roll angle. Because the spectra are ~ 100 pixels long, while the field size is 4096 pixels, the fraction of spectra truncated by the field edge (and thereby lost) is only $\sim 2\%$. A more detailed description of GRAPES project, especially the observations and the data reduction, can be found in Pirzkal et al. (2004). We note that the spectral resolution, line sensitivity, and equivalent width threshold for GRAPES emission lines are all comparable to typical modern narrowband surveys (e.g., Rhoads et al 2000, 2004; Rhoads & Malhotra 2001; Malhotra & Rhoads 2002; Cowie & Hu 1998; Hu et al 1998, 2002, 2004; Kudritzki et al 2000; Fynbo, Moller, & Thomsen 2001; Pentericci et al 2000; Stiavelli et al 2001; Ouchi et al 2001, 2003, 2004; Fujita et al 2003; Shimasaku et al 2003, 2006; Kodaira et al 2003; Ajiki et al 2004; Taniguchi et al 2005; Venemans et al 2002, 2004). However, the HST grism survey gives much broader redshift coverage and higher spatial resolution over a smaller solid angle. It yields immediate spectroscopic redshifts in many cases, and is immune to the strong redshift selection effects introduced in ground-based data by the forest of night sky OH emission lines.

After the data are reduced the spectra are extracted with the software package aXe¹. We search for the emission lines on all extracted spectra of the objects in the UDF field whose z-band (ACS F850LP filter) magnitudes reach as faint as $z_{AB} = 29$ mag. While the detection limit for continuum emission in the GRAPES spectra is brighter than this ($z_{AB} \approx 27.2$ mag; see Pirzkal et al. 2004), a fraction of such faint objects can have detectable emission lines.

¹ <http://www.stecf.org/software/aXe>

The emission line search for this paper was performed on the 1D extracted spectra, searching both in the spectra from individual PAs and on the combined spectra of all PAs.

To detect lines automatically, we wrote an IDL script (“emlinecull”) that identifies and fits lines as follows. We first remove the continuum by subtracting a median filtered version of the spectrum from the original data. We then determine whether the resulting high-pass filtered spectrum shows evidence for emission lines by sorting its pixels on signal to noise ratio and determining the maximum *net* signal to noise ratio in a running total of (1, 2, ..., N) pixels. (See Pirzkal et al. 2004 for further discussion of this “net significance” parameter applied to unfiltered 1D spectra.) In addition to “net significance,” we also calculate a cumulative continuum flux (based on the median spectrum that we subtracted). An object is retained as a likely emission line source provided that (a) its net significance exceeds 2.5, and (b) the ratio of “continuum” (i.e., low-pass filtered flux) to “line” (i.e., high-pass filtered flux) is ≤ 10 . The second criterion eliminates broad features of low equivalent width, thus avoiding a large catalog contamination by cool dwarf stars with “bumpy” continuum spectra. The precise line profile and other details affect the precise correspondence between this cutoff and a true equivalent width. This criterion will of course introduce some catalog incompleteness at low equivalent width, but this is inevitable anyway, given the limited spectral resolution of the grism.

Once an object is identified as a likely emission line source, the most significant peak in the filtered spectrum is identified, fitted with a Gaussian profile, and subtracted. This peak finding and subtraction is iterated until no pixel remaining in the residual spectrum exceeds the noise by a factor $> 2.5/\sqrt{2} = 1.77$. (This implies a net line significance $\gtrsim 2.5\sigma$ for any real selected line, since the line spread function is never narrower than two ACS pixels.) The output line list gives for each line the central wavelength, flux, line width, continuum level, and equivalent width, along with estimated uncertainties in each parameter. The fitting code is based on the IDL “MPFIT” package² written by Craig Markwardt.

The fitting code then checks the measured significance of each line, because line locations are initially based on the significance of single pixels, while the final significance is based on the full Gaussian fit to the line. At this stage we discard any candidate line whose final significance is $< 1.8\sigma$. Because this 1.8σ cutoff is applied in individual position angles, the final significance of a line after combining data from multiple GRAPES position angles (see below) will usually be $\gtrsim 3$. This step also discards any candidate lines with a fitted FWHM $< 10\text{\AA}$, because such narrow fitted widths are far below the instrumental resolution and therefore indicate a noise spike rather than a real spectral line.

² <http://cow.physics.wisc.edu/~craigm/idl/idl.html>

The observed line width is usually determined by the angular size of the object rather than its velocity width. Formally it is a convolution of the true emission line profile and the (projected) spatial profile of the object multiplied by the 40\AA per pixel dispersion. In general, this is dominated by the spatial term, unless the line width exceeds $30,000\text{ km s}^{-1} \times (\theta/\text{arcsec})$, where θ is the angular size of the object in the dispersion direction. Realistically, such extreme linewidth to size ratios are only expected in broad-lined active galactic nuclei (AGN). Here the observed spatial scale will be the PSF size ($0.1''$) regardless of distance, and the minimum velocity width for a resolved line becomes 3000 km s^{-1} .

After the emission line lists from individual PAs are generated through EmlineCull, we merge the lists according to following criteria: 1) A line is retained in one individual PA if the estimated contamination from overlapping spectra is less than 25% of the (line plus continuum) flux integrated over the line profile. Otherwise, if the estimated contamination exceeds 25%, the line is simply discarded. 2) Two lines from two different PAs are considered to be the same line if their wavelengths agree within their combined line widths (FWHM), after possible offsets between the cataloged object position and the location of strong line emitting regions are taken into account. 3) A line is considered as a detection if it is detected in at least 2 PAs. After this merged emission line object list is created, we visually examine all the individual spectra on both 1-dimensional extraction and 2-dimensional cut as a sanity check. This resulted in removal of some objects from the list. With the help of the emission line object list generated from the PA combined spectra, we also visually inspected all the combined spectra of the UDF objects down to and sometimes fainter than $i_{AB} = 28.0\text{ mag}$ as a completeness check. This resulted in the addition of a few emission line objects. Most of these were bright objects with broad emission lines of low equivalent width, which were missed in the automated line finding because they exceeded the threshold for continuum to line ratio.

Among the parameters returned by “emlinecull,” the central wavelength (and its associated error) are the most reliable. The other parameters are potentially affected by systematic effects. Line flux can be suppressed to some degree by the continuum subtraction procedure, and is furthermore underestimated due to aperture losses in the 1D extraction. The equivalent width is vulnerable to sky subtraction uncertainties for the faintest objects, and may also suffer if the spatial distribution of line emitting regions does not match that of continuum emitting regions, so that the equivalent width within the extracted aperture is not the correct spatially averaged equivalent width for the object. As discussed above, the line width is essentially a measure of object angular size for most objects. We have therefore chosen to report only the line wavelengths and approximate fluxes.

To improve the line flux estimates, we re-calculated them as follows. First we fit the

continuum to a pair of baseline regions, one on each side of the line, and subtract the resulting linear continuum fit from the spectrum. The typical width for the continuum fitting is about 2FWHM on each side of the line. We then do a direct integral of the continuum-subtracted line to determine its final flux estimate. Because we do not know the spatial distribution of line emitting regions in our sources *a priori*, we have chosen not to apply aperture corrections to the line fluxes. However, we can calculate what the aperture correction would be if the line flux were distributed like the continuum flux, using the direct images from the HUDF. To do so, we convolved the ACS i-band PSF with a gaussian of full width half maximum equal to the size of the object perpendicular to the grism direction, and then computed the fraction of the total flux falling within the grism extraction width. The resulting aperture corrections were factors of ~ 1.5 to ~ 3 , with a majority falling near the upper end of this range.

The final emission line object list is presented in Table 1. A total of 115 objects are listed in Table 1, of which 101 objects have UDF ID numbers from the released UDF catalogue. Those without UDF ID are either near a brighter object (with which they are blended in the UDF catalog) or else lie just outside the UDF field. Note that the GRAPES field of view covers a slightly larger area than that of UDF field due to the combination of exposures at different orientations. The total number of lines listed in Table 1 is 147, as multiple emission lines are detected in some galaxies.

The detected emission lines are then identified to the following template line list: a) Lyman- α ($\lambda 1216$); b) [O II] $\lambda 3727$; c) [O III] $\lambda 4959$ and [O III] $\lambda 5007$, which are not resolved at the ACS grism resolution ($\sim 40 \text{ \AA}/\text{pixel}$) below redshift 1.0 or for extended sources, so are treated as a single feature at [O III] $\lambda 4995$, their line ratio averaged wavelength; and d) H α ($\lambda 6563$). These lines are chosen because they are usually the strongest optical / near UV emission lines found in star forming galaxies. Some AGN emission lines are also used as a template in identifying AGNs. But the AGNs are identified primarily based on their point-like morphologies (Pirzkal et al. 2005).

The general line identification strategy is summarized as follows. 1) First we measure the photometric redshifts for all the objects in the list using the photo-z code (Mobasher et al. 2004). Only 4 objects outside the UDF field of view do not have photo-z measurements. Images from 7 filters are used to determine the redshift. These are: 4 ACS bands (BViz), 2 NICMOS bands (JH) and 1 ISAAC band (K). 2) We then use the photometric redshifts as the input to identify observed emission lines to the template lines and recalculate the redshift. If the recomputed redshift falls within the 95% confidence region of the photo-z redshift, we take it as measured redshift. 3) Visually examine all the line identifications. In last step, we have several different approaches: a) If an object is found to have 2 or more lines, we

calculate the wavelength ratio of different lines to re-identify the lines and recalculate the redshift if necessary. b) In both single and double emission line cases, if a relatively smooth break feature is found across the emission line region, it is very likely that this feature is the 4000 Å break, and the corresponding line can be identified as [O II] λ 3727. c) In the single emission line case, if a Lyman break feature is found near the emission line, and this Lyman break feature can be further confirmed with the broad band fluxes from the direct images, then the corresponding emission line is identified as Lyman- α . d) If a line cannot be identified with any method mentioned above, we simply present the measurements of the line without deriving its redshift. In the final list, 87% of the sample has line redshifts that are consistent with their photometric redshifts. Note that the GRAPES redshifts presented here do not in general provide an independent check on photometric redshift estimates, since a photometric redshift is used to help identify the emission lines in the GRAPES spectra. An exception can be made for objects with two GRAPES emission lines, in which case the wavelength ratio of the lines is usually measured with sufficient precision to identify them with no further information.

To assess the selection effects in our sample, we performed extensive Monte Carlo simulations of our line identification and measurement procedures. These simulations were performed in one dimension, using Bruzual & Charlot (2003) models for the continuum, with added emission lines. These lines were taken to be Gaussians with various widths and fluxes. We selected 100 Myr, 5 Myr, and 1.4 Gyr templates from the BC03 library, with metallicities of 0.08, 0.2 and 0.5 solar, thus yielding 9 different templates with a range of 4000Å break strengths and stellar absorption line strengths. In total, we simulated 1.5 million emission lines, spanning a wide range of continuum levels (e.g. scaled BC03 template), line fluxes, redshifts, and object sizes (which determine the effective resolution of each grism observation and the width of the observed lines). For each simulation, we stored the line flux, EW, i and z band broad band AB magnitude, redshift, and object size. Each of the simulated spectrum was multiplied by the ACS grism response function and resampled to the grism resolution of 40Å per pixel, prior to adding noise. Our noise calculation included both count noise from the input spectrum and the contribution of the sky background (≈ 0.1 DN/pixel/s), and was scaled to match the noise levels observed in the final, combined, GRAPES spectra. We identified spectral lines in each simulated spectrum using the same “emlinecull” script used to analyze the GRAPES data, and we determined a simulated line to be successfully detected if its measured line center was within one ACS grism resolution element (i.e. 40Å) of the simulated line center. Using these simulations, we were able to study the effect that wavelength, EW, line flux, object size, and line blending (in the case of 4959/5007Å) has on the fraction of successfully detected lines. Figure 1 shows the recovery fraction in the simulations for several input parameters. In each case, the remaining parameters are fixed

at values that allow for easy line identification.

Lyman- α presents a special case here because it is invariably located atop a significant spectral break when observed at the relevant redshifts. This means that the line not only needs to be significantly detected with respect to the photon noise ($s/n > 2.5$ as usual), but also must pass an equivalent width threshold that depends on the spectral resolution, in order to appear as a distinct emission line that the algorithm will identify. We characterized this effect by convolving a model spectrum of a Lyman- α emission line atop the corresponding Lyman- α break with line spread functions of width $60\text{\AA} \lesssim \Delta\lambda \lesssim 250\text{\AA}$, adding random noise, and running our detection algorithm. In the noise-free case, $EW \gtrsim 0.4\Delta\lambda$ is required for the line to be recovered. If we lower the continuum signal-to-noise ratio, the EW rises. The required equivalent widths for 80% completeness, given $s/n \approx 100, 10, 4.5, 2,$ and 1 per pixel in the continuum, become $\approx 0.5\Delta\lambda, 0.75\Delta\lambda, \Delta\lambda, 1.5\Delta\lambda,$ and $3\Delta\lambda$, respectively. In the limit of vanishingly small continuum, the problem reverts to detecting an isolated line, and for $s/n < 1$ per pixel, the threshold equivalent width scales as $1/(s/n)$ as expected.

3. Results

Table 1 lists a total of 115 galaxies that have detectable emission lines. Among these, 9 are high redshift Lyman- α emitters; at least 3 (and possibly up to 6) are active galactic nuclei (AGN); and the remainder are star forming galaxies detected in some combination of their [O II] $\lambda 3727$, [O III] $\lambda\lambda 4959, 5007$, and $H\alpha$ lines. In this latter category, 11 of them are detected with both [O II] $\lambda 3727$ and [O III] $\lambda\lambda 4959, 5007$ and 16 are detected with both [O III] $\lambda\lambda 4959, 5007$ and $H\alpha$. The first column of this table lists the UDF ID of the objects. An ID of “ ≤ -100 ” means that the object is outside or near the edge of the UDF field so it does not have a UDF ID. An ID between 0 and -100 means that the object is too close to an extended galaxy so it might be taken as part of that galaxy thus not assigned a UDF ID. The objects added into the line list after visual inspection of their spectra are marked with †. Column “i-mag” is the i-band AB magnitude of the object. Column “wavelength” is the central wavelength of the detected line, along with its 1σ statistical error estimate. Column “Line Flux” is line flux in the observed frame, as measured directly from the 1D spectra *without aperture correction*. The true line flux is in general larger by a factor of 1.5 to 3. Column “Redshift” is redshift determined from the emission lines, with a redshift of “-1” indicating that this line is not identified. Column “Line” is the physical identification of the observed line. Some examples of the emission line galaxy spectra are presented in figure 4.

Figure 5 shows the redshift distributions of the emission line galaxies according to the detected lines. The redshift range covered by each emission line is effectively set by the

wavelength coverage of the grism and the rest wavelengths of the lines. The grism response extends from 5500Å to 10500Å. In practice, we find we can detect emission lines usefully over the wavelength range $5700 \text{ \AA} \lesssim \lambda \lesssim 9700 \text{ \AA}$, which corresponds to a grism throughput $\gtrsim 25\%$ of the peak throughput. In this figure, a curve of the number (per redshift bin) of emission line galaxies that would be expected in the corresponding redshift (bin) are also overplotted. To derive these curves, we first generated a modified line luminosity function directly from the GRAPES data, using the $1/V$ method and the empirical sample, but disregarding both selection effects and evolution. We then used this function to estimate the number of objects that ought to have been detected in each redshift bin. The minimum luminosity for line detection was empirically calibrated to the faintest detected GRAPES emission lines, with the redshift dependence based on the grism sensitivity and the luminosity distance calculated in the current concordance cosmology ($\Omega_m = 0.3, \Omega_\Lambda = 0.7, H_0 = 70 \text{ km s}^{-1} \text{ Mpc}^{-1}$; see Spergel et al. 2003, 2006). The dotted curves are in some way an interpolation of the observed number-redshift counts, but they improve on a direct interpolation by incorporating our knowledge of the cosmology and instrument properties. Because the histograms are plotted based on detected lines, galaxies can contribute to more than one histogram if they have multiple detected emission lines.

4. Discussion

The GRAPES spectroscopy goes to much fainter continuum flux levels than is typical for ground-based followup spectroscopy. The median broad band magnitude for the emission line objects in table 1 is $i_{AB} = 24.67 \text{ mag}$ (see also figure 3). Over 40% of the sample has $i_{AB} > 25 \text{ mag}$, which is about the faintest magnitude level routinely targeted for ground-based followup spectroscopy, and 15% is fainter than $i_{AB} = 26 \text{ mag}$. It is thus likely that 30–40% of our emission line sample would be missed by ground-based followup efforts. The GRAPES sample thus provides a unique resource for studying emission line luminosity functions and the star formation rate density (SFRD) at moderate redshifts. The results of such studies will be presented in the companion paper (Gronwall et al. 2007). The morphologies of the emission line galaxies are presented in Pirzkal et al. (2006).

The 115 redshifts from this emission line catalog represent a fraction $\sim 5\%$ of the sources in the Hubble Ultra Deep Field brighter than 28th magnitude (AB). The primary factors leading to this comparatively small fraction are the selection effects demonstrated in figure 1. For an object to be selected in our emission line catalog with a reasonable probability, it must have $i_{AB} \lesssim 26.5$, $EW \gtrsim 50 \text{ \AA}$, size $< 0.75''$, and an emission line with observed wavelength $5800 \text{ \AA} \lesssim \lambda \lesssim 9600 \text{ \AA}$. Indeed, if we only consider objects with $i_{AB} < 26.5$, the redshift com-

pleteness rises to 9.5%. The GRAPES survey has also published continuum break redshifts of Lyman break galaxies (Malhotra et al 2005) and distant elliptical galaxies (Daddi et al 2005; Pasquali et al 2005), and there are additional redshift samples in progress for later type galaxies with 4000Å breaks (Hathi et al 2007, in preparation) and for an overarching sample of galaxies with significant spectroscopic continuum information in the GRAPES spectra (Ryan et al 2007, see below). So the spectroscopic success rate is reasonably high for sources where sufficient information can be expected given the properties of the instrument and data set. In particular, the fraction of redshifts lost to crowding and overlap is modest, because of our multiple roll angle observing strategy.

As a sanity check, we compared our measured redshifts with those available in the Chandra Deep Field South and found good agreement. We use redshifts from five available references (Vanzella et al. 2005; Le Fevre et al. 2005, Szokoly et al. 2004, Vanzella et al. 2006, and Grazian et al. 2006). The results of this comparison are given in table 2. Both the overall agreement and the agreement with individual references was generally good. For example, we found that there are 7 objects in common in our emission line catalog and the VLT/FORS2 catalog of Vanzella et al. 2005. Among these, redshifts are in agreement for 6 objects. Moreover, the one that does not agree, UDF -100, also shows up in Le Fevre et al. 2004, where its redshift *does* agree with our measurement. Among the 9 objects in Le Fevre, only one (UDF3484) disagrees. We also found 4 out of 5 in agreement with Szokoly et al. 2004 (here the object that does not agree is UDF4445, a 2-line object). The total sample is 23 objects with both GRAPES and ground-based redshifts available. Among these, 2.5 show “catastrophic” redshift mismatches (where the “0.5” object is our ID -100, with two inconsistent ground-based redshifts). This 11% failure rate is essentially the same as the catastrophic failure rate for photometric redshifts, and for essentially the same reason: Most of our redshifts are constrained to match a photometric redshift at the outset. The catastrophic failures in our list correspond to mis-identified emission lines.

In a future paper (Ryan et al 2007) we will combine the continuum shape information from the grism with multi-band optical and near-IR photometry to derive spectrophotometric redshifts for the GRAPES data set. This effort may reduce the catastrophic failure rate in line identifications, since the extra information from the grism continuum will help distinguish among the redshift likelihood peaks in photometric redshift fitting.

To estimate our redshift accuracy, we study the cleanest subset of these object with ground-based and GRAPES redshifts. We first exclude the catastrophic failures from consideration (excluding ID -100 along with the other two). Our catalog also has a few lines from the manually identified emission line galaxies where we lack an automated line wavelength uncertainty estimate, and we exclude these also for the present. Among the remaining

15 overlap objects, the RMS redshift difference between GRAPES and ground-based data is $\text{RMS}(\Delta z) = 0.008$. For comparison, the median estimated redshift uncertainty from our line centroiding algorithm is $\text{median}(\delta\lambda/\lambda_{rest}) = 0.009$. Thus, we infer a typical redshift uncertainty just below 0.01 for our emission line catalog. Examining the redshift residuals $z_{GRAPES} - z_{VLT}$ as a function of redshift shows weak evidence for a systematic offset at $z \lesssim 0.3$, with $\langle z_{GRAPES} - z_{VLT} \rangle \sim 0.01$, but this is based on only 3 or 4 data points and may be a coincidence.

If we examine our subsample with two emission lines and compare the redshifts derived separately from the two lines, we reach a similar conclusion– the offset between these measurements is again fully consistent with characteristic redshift errors $\delta z \lesssim 0.01$.

The comparison with ground-based spectra also allows us to estimate the systematic error floor in our line wavelength measurements: A systematic error component of $\sim 12\text{\AA}$ is quite sufficient to account for the observed redshift offset between ground and GRAPES data for those lines whose formal wavelength uncertainty $\delta\lambda < 5\text{\AA}$. A larger comparison sample might refine this estimate, but is unlikely to change it dramatically.

5. Conclusion

We find that a deep spectroscopic survey like GRAPES offers a unique opportunity to identify emission lines and determine redshifts for faint galaxies. In this paper, we present a catalog of emission lines identified in GRAPES, including wavelength measurements, flux estimates, line identifications, and redshifts. Over 40% of the sample comes from objects fainter than the typical continuum magnitude limit for ground-based multiobject spectroscopic followup programs. These objects might never have been identified as emission line galaxies without a space based observation as ours. Based on comparison with ground-based spectra for a subset of our objects, we infer a typical redshift accuracy of $\delta z = 0.009$ for our catalog.

This work was supported by grant GO-09793.01-A from the Space Telescope Science Institute, which is operated by AURA under NASA contract NAS5-26555. ED acknowledge support from NASA through the Spitzer Fellowship Program, under award 1268429. This project has made use of the aXe extraction software, produced by ST-ECF, Garching, Germany. We also made use of the "mpfit" IDL library, and we thank Craig Markwardt for making this package public.

REFERENCES

- Ajiki, M., et al 2004, PASJ 56, 597
- Beckwith, S.V.W., et al. 2006, in preparation
- Bertin, E., & Arnouts, S., A&AS, 117, 393
- Bruzual A., G., & Charlot, S. 2003, MNRAS, 344, 1000
- Cowie, L. L., & Hu, E. M. 1998, AJ, 115, 1319
- Daddi, E., et al. 2005, ApJ, 626, 680
- Drozdovsky, I., Yan, L, Chen, H.-W., Stern, D., Kenicutt, R., Spinrad, H., & Dawson, S. 2005, AJ, 130, 1324
- Francis, P., et al 1991, ApJ, 373, 465
- Fujita, S. S., et al 2003, ApJ, 586, L115
- Fynbo, J. U., Moller, P., & Thomsen, B. 2001, A&A, 374, 443
- Gallego, J., Zamorano, J., Aragon-Salamanca, A., & Rego, M 1995, ApJ, 455, L1
- Gallego, J., García-Dabó, C. E., Zamorano, J., Aragón-Salamanca, A., & Rego, M 2002, ApJ, 570, L1
- Grazian, A., Fontana, A., De Santis, C., et al 2006, A&A, in press; astro-ph/0603094
- Gronwall, C., et al. 2007, in preparation
- Hathi, N. et al 2007, in preparation.
- Hu, E. M., Cowie, L. L., & McMahon, R. G. 1998, ApJ, 502, L99
- Hu, E. M., et al. 2002, ApJ, 568, L75
- Hu, E. M., Cowie, L. L., Capak, P., McMahon, R. G., Hayashino, T., Komiyama, Y. 2004, AJ, 127, 563
- Izotov, Y.I., & Thuan, T. X. 1999, ApJ, 511, 639
- Kodaira, K. et al. 2003, PASJ, 55, L17
- Koo, D.C., & Kron, R.T., 1980, PASP, 92, 537

- Kudritzki, R.-P. et al. 2000, ApJ, 536, 19
- Le Fevre, O., Vettolani, G., Paltani, S., et al. 2004, A&A, 428, 1043
- MacAlpine, G. M., Smith, S. B., & Lewis, D. W. 1977, ApJS, 34, 95
- MacAlphine, G. M., & Williams, G. A. 1981, ApJS, 45, 113
- Malhotra, S., & Rhoads, J.E., 2002, ApJ, 565, L71
- Malhotra, S., & Rhoads, J.E., 2004, ApJ, 617, L5
- Malhotra, S., et al. 2005, ApJ, 626, 666
- Malhotra, S., & Rhoads, J.E., 2006, ApJ, 647, L95; astro-ph/0511196
- McCarthy, P. J., et al. 1999, ApJ, 520, 548
- Mobasher, B., Idzi, R., Benítez, N., et al. 2004, ApJ, 600L, 167
- Ouchi, M. et al. 2001, ApJ, 558, 83
- Ouchi, M. et al. 2003, ApJ, 582, 60
- Ouchi, M. et al. 2004, ApJ, 611, 685
- Pasquali, A., Larsen, S., Ferreras, I., Gnedin, O. Y., Malhotra, S., Rhoads, J., Pirzkal, N., & Walsh, J. 2005, AJ, 129, 148
- Pentericci, L. et al. 2000, A&A, 361, 25
- Pasquali, A., et al 2006, ApJ 636, 115
- Pirzkal, N., Xu, C., Malhotra, S., et al. 2004, ApJS, 154, 501
- Pirzkal, N., et al. 2005, ApJ, 622, 319
- Pirzkal, N., et al. 2006, ApJ 636, 582
- Pritchett, C.J., 1994, PASP, 106, 1052
- Rhoads, J. E., Malhotra, S., Dey, A., Stern, D., Spinrad, H., & Jannuzi, B. T. 2000, ApJ, 545, L85
- Ryan, R., et al 2007, in preparation.
- Rhoads, J. E., & Malhotra, S., 2001, ApJ 563, L5

- Rhoads, J. E., Xu, C., Dawson, S., Dey, A., Malhotra, S., Wang, J. X., Jannuzi, B. T., Spinrad, H., & Stern, D. 2004, *ApJ*, 611, 59
- Salzer, J. J., et al. 2000, *AJ*, 120, 80
- Shimasaku, K. et al. 2003, *ApJ*, 586, L111
- Shimasaku, K. et al. 2006, *PASJ*, 58, 313
- Smith, M. G. 1975, *ApJ*, 202, 591
- Smith, M. G., Aguirre, C., & Zemelmann, M. 1976, *ApJS*, 32, 217
- Spergel, D. N., et al. 2003, *ApJS*, 148, 175
- Spergel, D. N., et al. 2006, *ApJ*, submitted (astro-ph/0603449)
- Stiavelli, M., Scarlata, C., Panagia, N., Treu, T., Bertin, G., & Bertola, F. 2001, *ApJ*, 561, L37
- Szokoly, G.P., Bergeron, J., Hasinger, G., et al. 2004, *ApJS*, 155, 271
- Taniguchi, Y. et al 2005, *PASJ*, 57, 165
- Teplitz, H.I., Malkan, M.A., Steidel, C.C., et al. 2000, *ApJ*, 542, 18
- Teplitz, H. I., Collins, N. R., Gardner, J. P., Hill, R. S., Heap, S. R., Lindler, D. J., Rhodes, J., & Woodgate, B. E. 2003, *ApJS*, 146, 209
- Teplitz, H. I., Collins, N. R., Gardner, J. P., Hill, R. S., & Rhodes, J. 2003, *ApJ*, 589, 704
- vanden Berk, D., et al 2001, *AJ*, 122, 549
- Vanzella, E., Cristiani, S., Dickinson, M., et al. 2005, *A&A*, 434, 53
- Vanzella, E., Cristiani, S., Dickinson, M., et al. 2006, *A&A*, submitted; astro-ph/0601367
- Venemans, B. P. et al. 2002, *ApJ*, 569, L11
- Venemans, B. P. et al. 2004, *A&A*, 424, L17
- Yan, L., McCarthy, P. J., Freudling, W., Teplitz, H. I., Malumuth, E. M., Weymann, R. J., & Malkan, M. A. 1999, *ApJ*, 519, L47
- Zamorano, J., Rego, M., Gallego, J. G., Vitores, A. G., Gonzalez-Riestra, R., & Rodriguez-Caderot, G. 1994, *ApJS*, 95, 387

Zamorano, J., Gallego, J., Rego, M., Vitores, A. G., & Alonso, O. 1996, ApJS, 105, 343

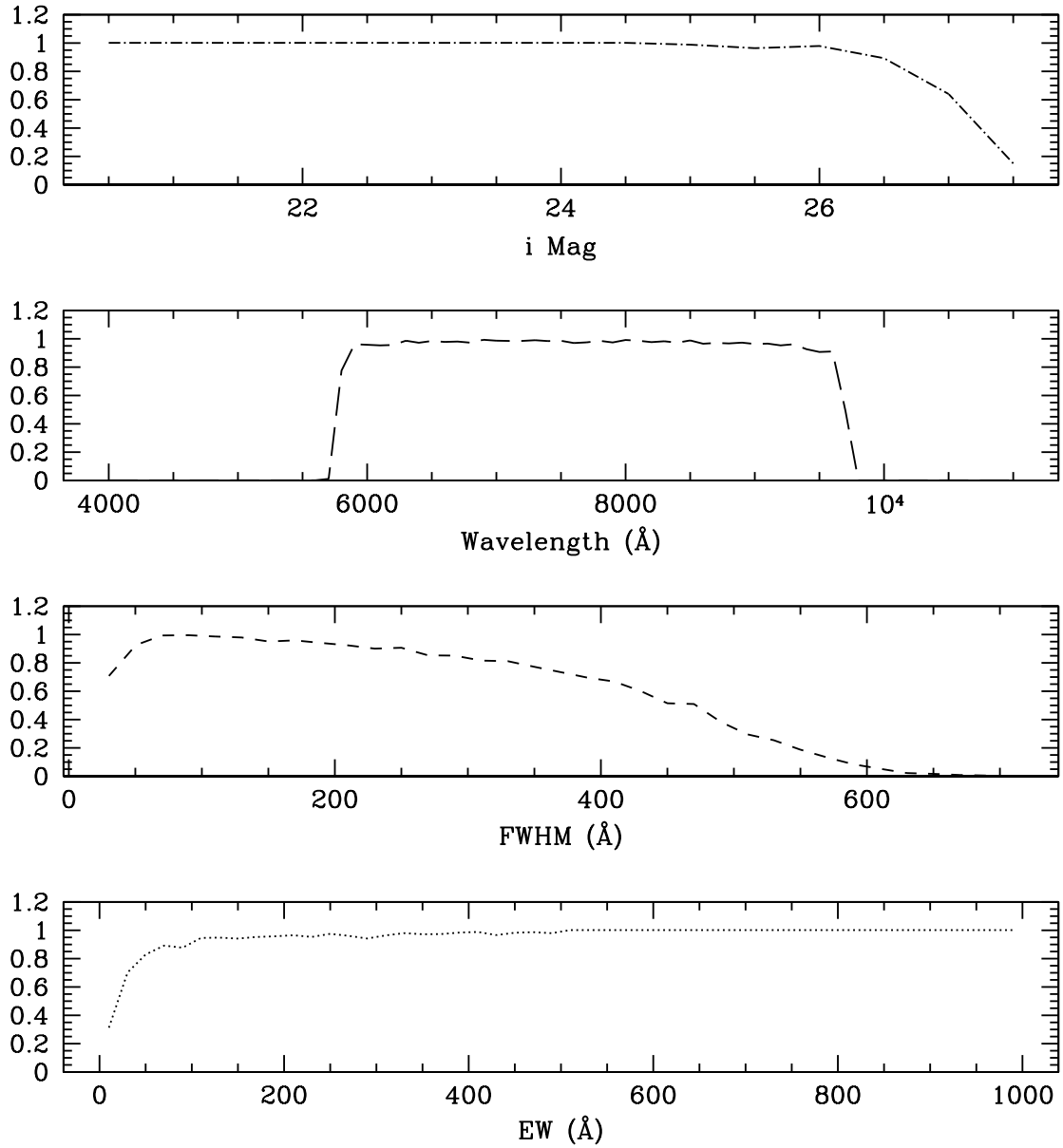


Fig. 1.— The line recovery rate based on different line width, equivalent width, central wavelength and host galaxy brightness. In each panel, the parameter shown on the x axis is allowed to vary, while the remaining input parameters are fixed at values that are generally favorable for line detections.

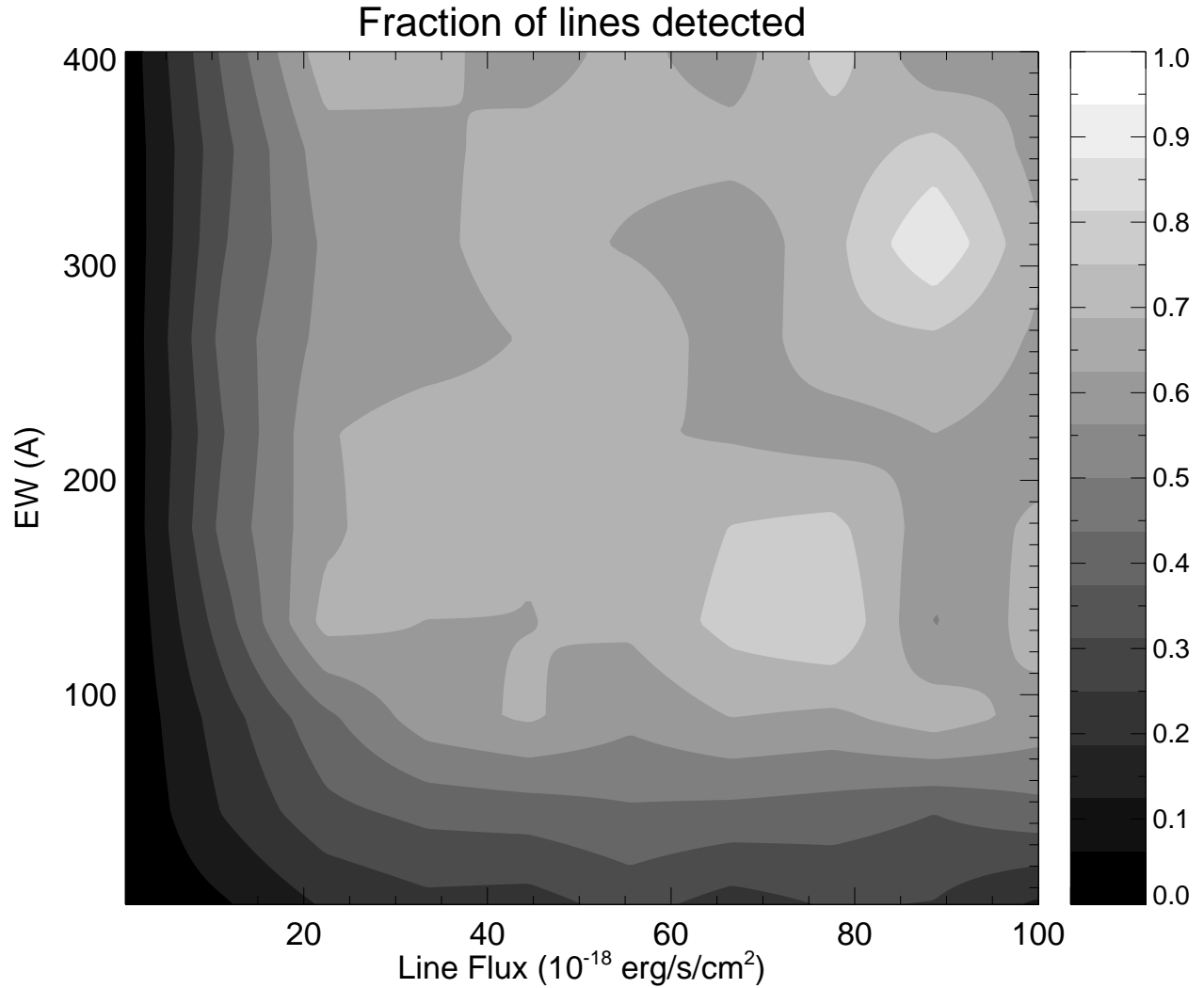


Fig. 2.— The line recovery rate as a two-dimensional function of line flux and equivalent width. In this figure (unlike figure 1), the other relevant parameters are allowed to vary over a wide range. Thus, the “plateau” region in the contour plot with selection probability $\gtrsim 60\%$ corresponds to the region where the EW and line flux are sufficient for selection. Those lines *not* recovered in this portion of the plot were missed due to an unfavorable choice of line width or wavelength.

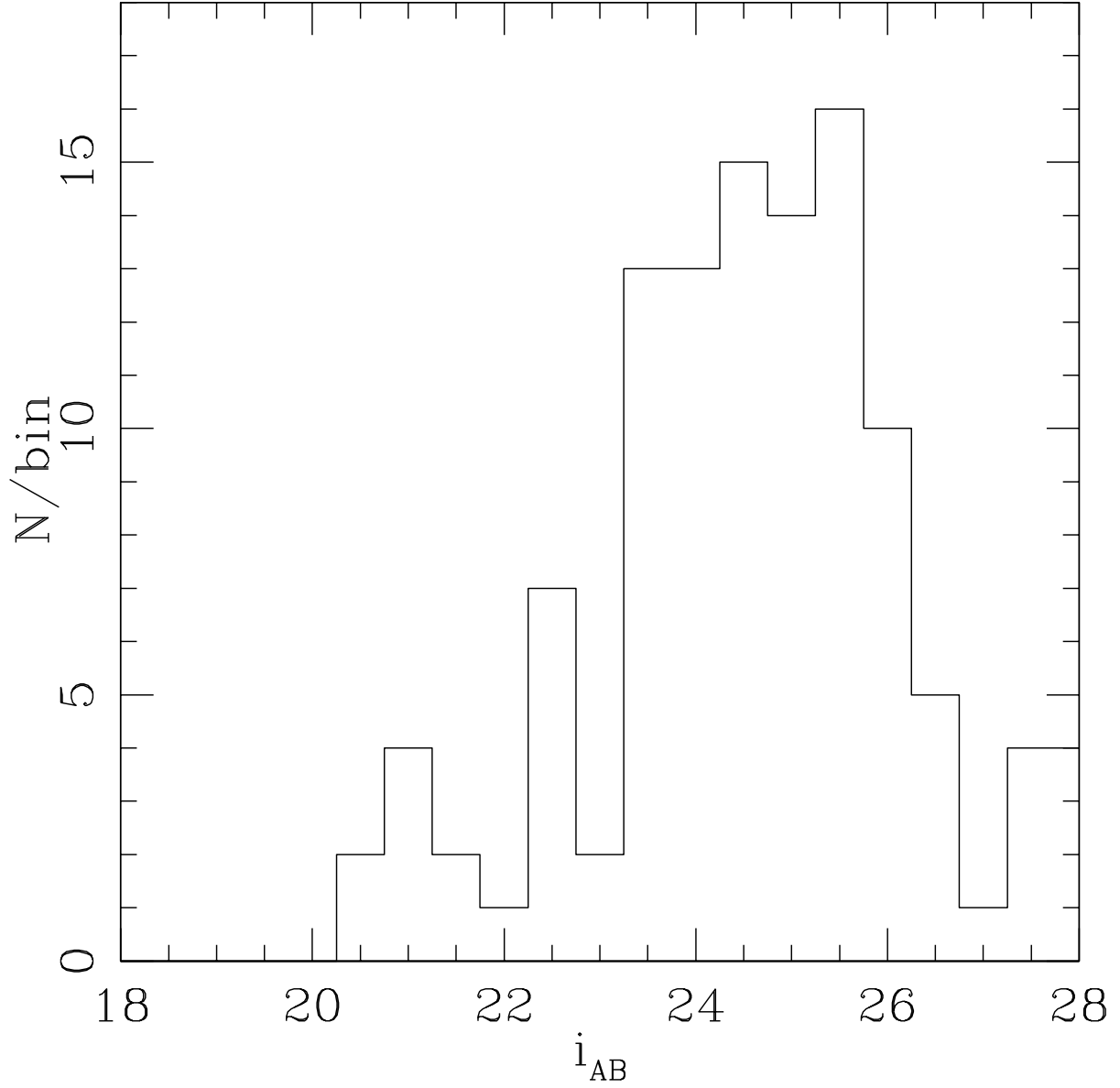


Fig. 3.— The histogram of i-band magnitude of all the emission line objects listed in Table 1. The binsize of the histogram is 0.5 magnitude.

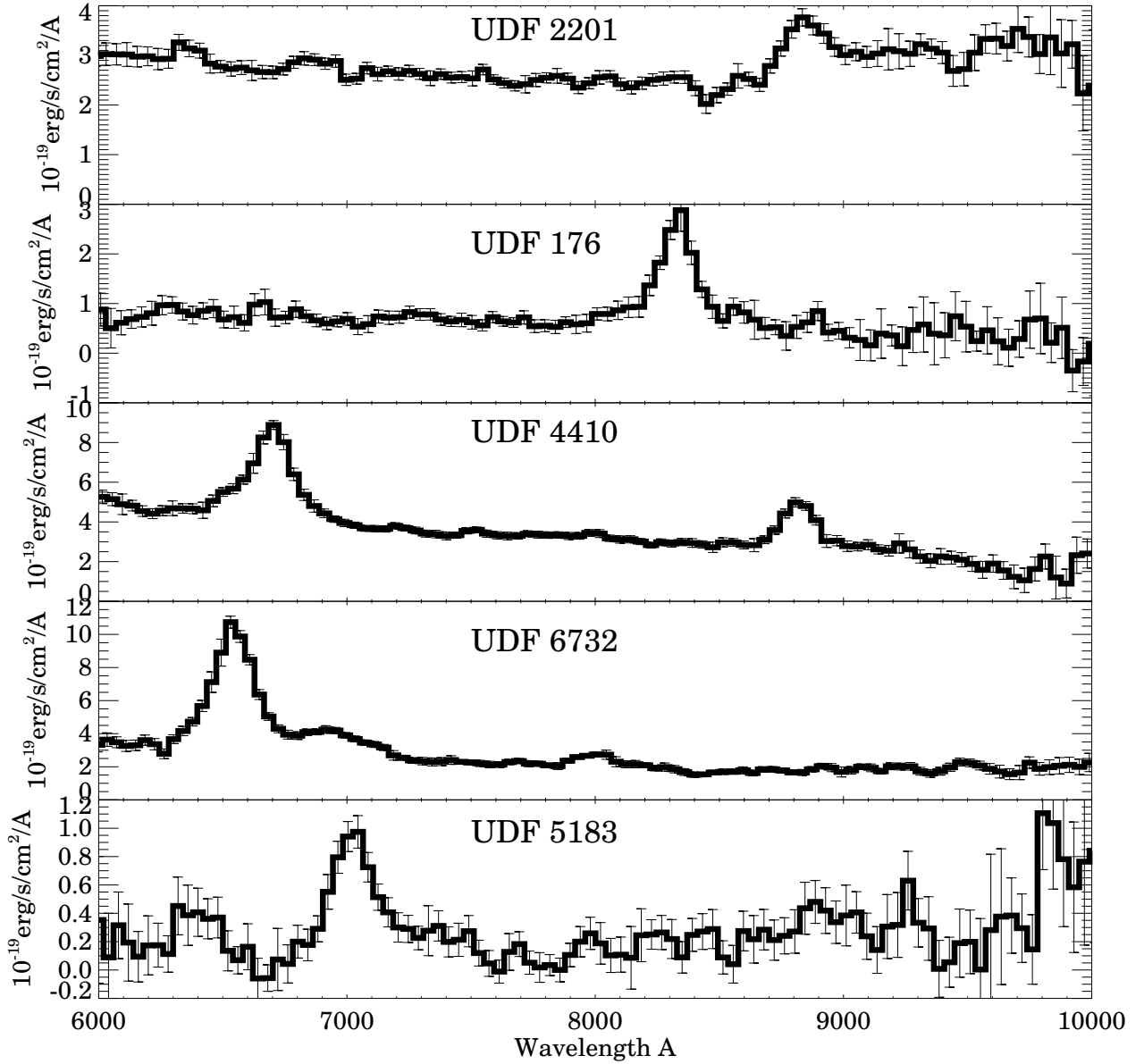


Fig. 4.— Some examples of the ACS grism spectra from the emission line galaxy catalog. From the top to the bottom panels are: UDF 2201, with [O II] $\lambda 3727$ at $z = 1.377$; UDF 176, with [O III] $\lambda\lambda 4959, 5007$ at $z = 0.667$; UDF 4410, with [O III] $\lambda\lambda 4959, 5007$ and $H\alpha$ at $z = 0.346$; UDF 6732, a quasar with [C IV] $\lambda 1549$ and [C III] $\lambda 1909$ at $z = 3.19$; and UDF 5183, a Ly α emitter at $z = 4.78$. The apparent continuum level in UDF 5183 (at magnitude $i_{AB} \approx 27.4$ mag) should be treated with caution, as it is below the systematic error level in GRAPES sky subtraction (a few $\times 10^{-4}$ counts/sec/pixel; see Pirzkal et al 2004).

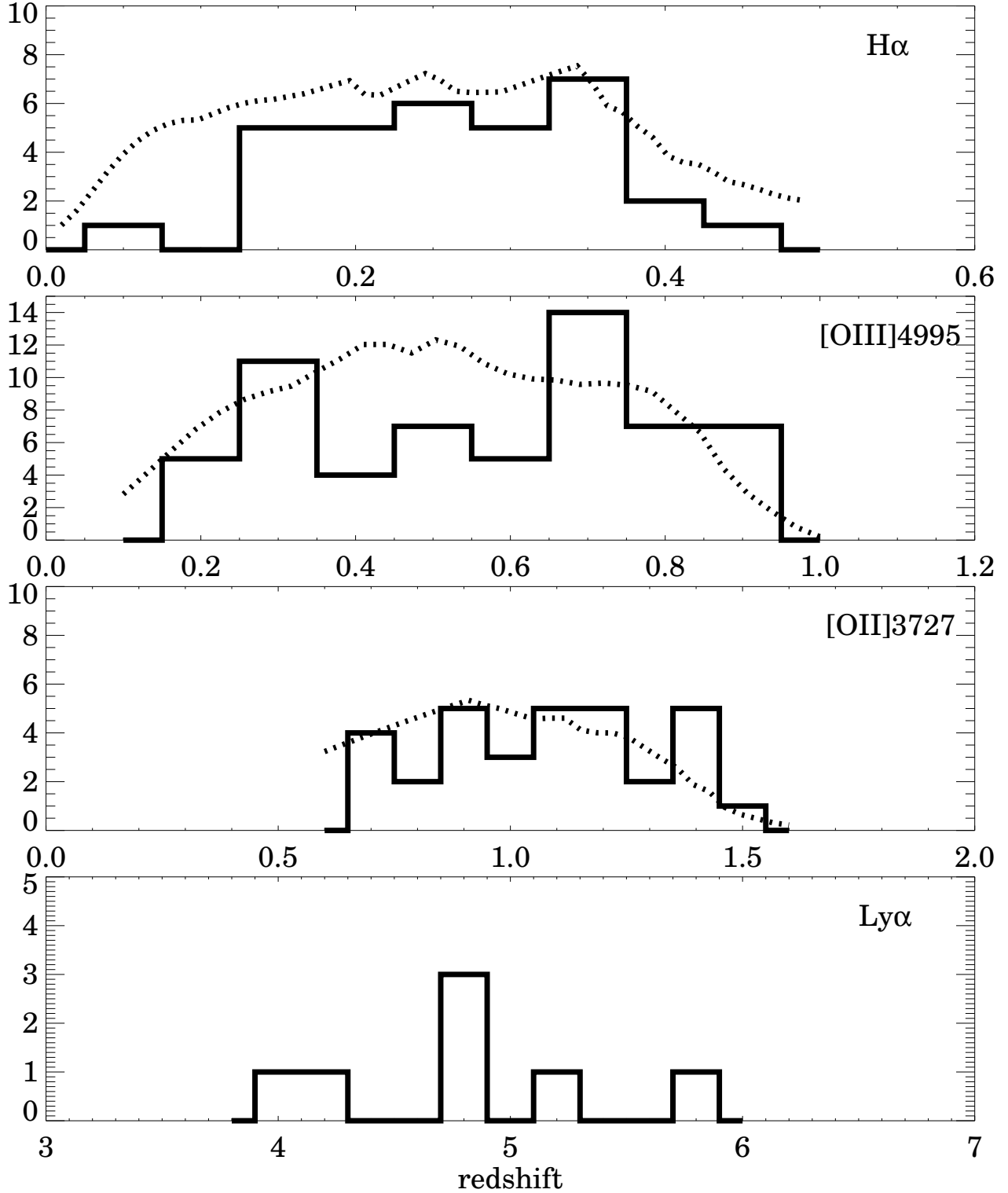


Fig. 5.— The distribution of the redshifts from different lines. From top panel to the bottom are $H\alpha$, [O III] $\lambda\lambda 4959, 5007$, [O II] $\lambda 3727$ and $Ly\alpha$. Their binsize in redshift z are 0.05, 0.1, 0.1 and 0.2 respectively. Each histogram is overplotted with the number of objects that would be expected in that bin based on the minimum line luminosity required for detection as a function of redshift and rest wavelength, and on line luminosity functions derived directly from GRAPES data. Comparing the observed redshift histogram with this curve allows us to identify overdense and underdense regions along the line of sight. While individual peaks are not strongly significant given our sample size, we note that the peak at $z \approx 0.7$ in the [O III] $\lambda 5007$ redshift distribution corresponds to two closely spaced peaks that have been previously noted in the CDF-South field at $z \approx 0.67$ and $z \approx 0.73$ (Vanzella et al 2005).

Table 1. Emission Line Objects in UDF Field

UDF ID	RA	DEC	i-mag (AB)	Wavelength ^a Å	Measured Line Flux ^b $10^{-18} \text{erg/s/cm}^2$	Redshift	Line
-100 [†]	53.1773491	-27.7639294	22.439	7995.7 ± 6.7	105	0.601	[OIII] $\lambda\lambda$ 4959,5007
-101	53.1878090	-27.7726192	22.681	7470.4 ± 37.3	107	0.138	H α
-102	53.2072487	-27.7847309	23.884	7617.9 ± 42.3	18	0.161	H α
-103	53.1970100	-27.7805996	24.127	6485.5 ± 32.2	24	0.740	[OII] λ 3727
				8721.9 ± 42.1	18	0.746	[OIII] $\lambda\lambda$ 4959,5007
-104 [†]	53.1931000	-27.7755508	25.233	8265.5 ± 1.4	13	1.218	[OII] λ 3727
-105	53.1855392	-27.8111000	24.417	6663.6 ± 28.0	7	0.334	[OIII] $\lambda\lambda$ 4959,5007
				8748.8 ± 32.2	17	0.333	H α
-106	53.1649399	-27.7558804	25.263	7535.7 ± 41.3	19	-1.000	
-107 [†]	53.1795387	-27.7661705	25.057	8336.5 ± 22.0	34	0.669	[OIII] $\lambda\lambda$ 4959,5007
-108 [†]	53.1948090	-27.7733498	25.576	8063.1 ± 6.5	27	0.614	[OIII] $\lambda\lambda$ 4959,5007
-109 [†]	53.1554108	-27.8261108	25.431	8009.8 ± 11.2	37	0.604	[OIII] $\lambda\lambda$ 4959,5007
-110	53.1681290	-27.7565002	25.536	7867.2 ± 44.0	18	-1.000	
-1	53.1843987	-27.8051605	25.383	6253.9 ± 41.2	11	0.678	[OII] λ 3727
				8347.4 ± 29.9	20	0.671	[OIII] $\lambda\lambda$ 4959,5007
33	53.1632500	-27.8267040	25.591	9201.5 ± 50.5	14	0.842	[OIII] $\lambda\lambda$ 4959,5007
119	53.1660042	-27.8238735	27.364	7388.9 ± 47.9	7	0.479	[OIII] $\lambda\lambda$ 4959,5007
166	53.1605415	-27.8226891	25.650	8104.6 ± 38.7	6	1.897	[MgII] λ 2798
176	53.1583786	-27.8228283	25.728	8327.0 ± 39.4	27	0.667	[OIII] $\lambda\lambda$ 4959,5007
178	53.1610794	-27.8219051	23.753	8313.5 ± 43.3	27	0.664	[OIII] $\lambda\lambda$ 4959,5007
206	53.1717300	-27.8217850	23.503	7181.3 ± 25.4	9	0.927	[OII] λ 3727
				9642.8 ± 27.3	76	0.930	[OIII] $\lambda\lambda$ 4959,5007
631	53.1670227	-27.8169975	26.463	6234.5 ± 17.9	20	4.127	Ly α
648	53.1607285	-27.8162994	24.754	7492.2 ± 32.0	16	0.142	H α

Table 1—Continued

UDF ID	RA	DEC	i-mag (AB)	Wavelength ^a Å	Measured Line Flux ^b $10^{-18} \text{ erg/s/cm}^2$	Redshift	Line
703	53.1734314	-27.8157158	24.618	8547.7 ± 30.0	20	0.711	[OIII] $\lambda\lambda$ 4959,5007
704	53.1788826	-27.8159561	25.221	8692.8 ± 36.6	11	0.740	[OIII] $\lambda\lambda$ 4959,5007
712	53.1783562	-27.8162518	27.296	7537.0 ± 49.1	6	5.198	Ly α
900 [†]	53.1851387	-27.8052711	20.354	9313.6 ± 4.3	280	0.419	H α
1000	53.1531181	-27.8120880	23.301	6135.2 ± 43.8	39	0.228	[OIII] $\lambda\lambda$ 4959,5007
				8083.0 ± 51.2	56	0.231	H α
1016	53.1813507	-27.8126469	25.761	6860.1 ± 38.9	6	0.841	[OII] λ 3727
				9155.1 ± 30.6	32	0.833	[OIII] $\lambda\lambda$ 4959,5007
1309 [†]	53.1512070	-27.8095436	24.600	8296.3 ± 17.2	23	-1.000	
1322	53.1506081	-27.8094997	24.624	6563.8 ± 52.6	6	0.314	[OIII] $\lambda\lambda$ 4959,5007
				8606.7 ± 21.7	33	0.311	H α
1344	53.1536598	-27.8089428	23.835	6805.2 ± 59.6	13	0.037	H α
1347	53.1510468	-27.8094597	24.665	7753.5 ± 32.2	5	1.080	[OII] λ 3727
1446	53.1632233	-27.8089867	26.509	9226.4 ± 44.6	10	2.470	
1752	53.1705093	-27.8066654	25.246	8341.0 ± 25.6	10	1.238	[OII] λ 3727
1889	53.1732178	-27.8061523	25.852	9063.5 ± 26.5	17	1.432	[OII] λ 3727
2088	53.1540489	-27.8051834	26.694	8329.9 ± 39.7	9	0.668	[OIII] $\lambda\lambda$ 4959,5007
2162	53.1487541	-27.8043003	24.029	7135.4 ± 49.6	23	0.914	[OII] λ 3727
				9578.8 ± 40.2	60	0.918	[OIII] $\lambda\lambda$ 4959,5007
2201	53.1416206	-27.8040810	24.428	8859.2 ± 43.4	15	1.377	[OII] λ 3727
2241	53.1377258	-27.8042164	25.860	7674.1 ± 40.6	26	0.536	[OIII] $\lambda\lambda$ 4959,5007
2848	53.1472511	-27.8008347	26.087	6378.2 ± 28.0	26	0.277	[OIII] $\lambda\lambda$ 4959,5007
				8385.9 ± 25.0	11	0.278	H α
2927	53.1478958	-27.7996979	23.945	7274.1 ± 44.5	7	0.456	[OIII] $\lambda\lambda$ 4959,5007

Table 1—Continued

UDF ID	RA	DEC	i-mag (AB)	Wavelength ^a Å	Measured Line Flux ^b $10^{-18} \text{ erg/s/cm}^2$	Redshift	Line
2974	53.1733017	-27.7992401	23.668	7564.0 ± 28.7	24	0.153	H α
				9569.9 ± 56.0	37	-1.000	
2998	53.1512070	-27.7987099	23.647	8023.2 ± 49.3	38	0.222	H α
3068	53.1781006	-27.7999439	25.940	8461.9 ± 38.3	13	1.270	[OII] λ 3727
3484	53.1980057	-27.7967453	23.088	7017.6 ± 72.1	25	0.405	[OIII] $\lambda\lambda$ 4959,5007
3823	53.1613274	-27.7958012	24.431	9266.9 ± 32.9	15	1.486	[OII] λ 3727
3869	53.1880836	-27.7957401	24.232	7063.7 ± 41.5	13	0.414	[OIII] $\lambda\lambda$ 4959,5007
3914	53.1873589	-27.7942257	22.549	6660.7 ± 28.3	256	0.333	[OIII] $\lambda\lambda$ 4959,5007
				8815.1 ± 32.8	166	0.343	H α
3959	53.1794853	-27.7960243	28.023	9203.7 ± 45.5	4	0.843	[OIII] $\lambda\lambda$ 4959,5007
3977	53.1558685	-27.7949009	23.462	7833.1 ± 39.4	17	1.102	[OII] λ 3727
4029	53.1663704	-27.7956104	26.729	7688.9 ± 30.6	10	0.539	[OIII] $\lambda\lambda$ 4959,5007
4084	53.1278381	-27.7947979	24.050	7868.7 ± 32.3	5	1.111	[OII] λ 3727
4120	53.1839104	-27.7954140	27.876	8661.0 ± 32.6	19	2.095	[MgII] λ 2798
4126	53.1541138	-27.7950897	25.988	8622.6 ± 41.1	12	0.726	[OIII] $\lambda\lambda$ 4959,5007
4142 [†]	53.1841469	-27.7926502	21.628	6437.1 ± 0.0	51	0.727	[OII] λ 3727
				8635.1 ± 0.0	148	0.729	[OIII] $\lambda\lambda$ 4959,5007
4172	53.1255722	-27.7949314	25.835	8789.3 ± 38.5	8	1.358	[OII] λ 3727
4262	53.1619377	-27.7925472	22.748	7316.5 ± 41.1	61	0.465	[OIII] $\lambda\lambda$ 4959,5007
4315	53.1546211	-27.7932377	22.668	6150.1 ± 11.1	11	0.231	[OIII] $\lambda\lambda$ 4959,5007
				8081.0 ± 7.8	20	0.231	H α
4371	53.1822014	-27.7939930	24.954	8614.0 ± 39.2	13	0.725	[OIII] $\lambda\lambda$ 4959,5007
4396	53.1491623	-27.7929745	24.445	8266.3 ± 40.0	17	1.218	[OII] λ 3727
4410	53.2002335	-27.7937489	24.158	6720.9 ± 38.9	92	0.345	[OIII] $\lambda\lambda$ 4959,5007

Table 1—Continued

UDF ID	RA	DEC	i-mag (AB)	Wavelength ^a Å	Measured Line Flux ^b $10^{-18} \text{ erg/s/cm}^2$	Redshift	Line
				8848.0 ± 33.8	40	0.348	H α
4442	53.1640625	-27.7942142	29.564	8221.0 ± 29.4	7	5.761	Ly α
4445	53.1615601	-27.7922573	21.130	7178.4 ± 42.4	137	0.926	[OII] λ 3727
				9599.8 ± 17.5	705	0.922	[OIII] $\lambda\lambda$ 4959,5007
4496	53.1530037	-27.7936897	26.546	8599.2 ± 74.1	19	1.307	[OII] λ 3727
4816	53.1840210	-27.7915077	24.560	8311.0 ± 33.0	12	1.230	[OII] λ 3727
4825	53.1673279	-27.7918644	23.961	6698.5 ± 14.6	14	0.341	[OIII] $\lambda\lambda$ 4959,5007
				8781.7 ± 22.8	7	0.338	H α
4929 [†]	53.1879463	-27.7900028	20.792	9436.0 ± 0.0	590	0.438	H α
4981	53.1444244	-27.7911167	24.692	9056.2 ± 28.1	6	1.430	[OII] λ 3727
5183	53.1437798	-27.7908649	27.417	7032.9 ± 39.8	11	4.784	Ly α
5187	53.1848183	-27.7899323	23.702	7313.1 ± 27.0	14	0.962	[OII] λ 3727
5225 ^c	53.1385743	-27.7902115	25.953	7933.2 ± 33.9	22	5.42	Ly α
5399	53.1764984	-27.7897053	24.981	7095.1 ± 29.3	36	0.420	[OIII] $\lambda\lambda$ 4959,5007
				9322.7 ± 35.1	13	0.421	H α
5435	53.1508255	-27.7896385	25.566	8031.3 ± 41.2	8	0.224	H α
5491	53.1956520	-27.7877655	22.191	5970.6 ± 25.1	682	0.195	[OIII] $\lambda\lambda$ 4959,5007
				7892.5 ± 48.2	297	0.203	H α
5569	53.1471786	-27.7884827	23.317	6185.3 ± 25.0	23	0.660	[OII] λ 3727
				8254.0 ± 25.9	60	0.652	[OIII] $\lambda\lambda$ 4959,5007
5606 [†]	53.1421242	-27.7866974	20.719	8229.4 ± 0.0	214	0.254	H α
5620	53.1815414	-27.7879868	23.327	6172.1 ± 35.4	42	0.236	[OIII] $\lambda\lambda$ 4959,5007
				8044.7 ± 16.4	52	0.226	H α
5815	53.1983261	-27.7878132	25.955	9426.5 ± 29.6	12	0.887	[OIII] $\lambda\lambda$ 4959,5007

Table 1—Continued

UDF ID	RA	DEC	i-mag (AB)	Wavelength ^a Å	Measured Line Flux ^b $10^{-18} \text{ erg/s/cm}^2$	Redshift	Line
5933	53.1782417	-27.7872906	25.379	6742.2 ± 31.6	23	0.350	[OIII] $\lambda\lambda$ 4959,5007
				8836.6 ± 22.5	10	0.346	H α
5959	53.1640968	-27.7872963	24.325	7831.5 ± 27.3	33	0.193	H α
6022	53.1471252	-27.7871094	25.249	8891.0 ± 26.5	3	0.780	[OIII] $\lambda\lambda$ 4959,5007
6082	53.1447182	-27.7854404	22.470	6131.5 ± 13.4	953	0.228	[OIII] $\lambda\lambda$ 4959,5007
				8177.0 ± 16.7	392	0.246	H α
6139	53.1581268	-27.7863865	25.559	7145.9 ± 63.1	22	4.877	Ly α
6162	53.1634712	-27.7866364	25.340	7388.6 ± 27.8	16	0.479	[OIII] $\lambda\lambda$ 4959,5007
6196	53.1604767	-27.7862968	24.792	7387.6 ± 29.3	4	0.982	[OII] λ 3727
6710	53.1925850	-27.7838020	25.017	9301.4 ± 32.7	4	0.862	[OIII] $\lambda\lambda$ 4959,5007
6732	53.1784897	-27.7840405	24.625	6494.7 ± 48.6	137	3.193	[CIV] λ 1549
				7991.4 ± 22.8	25	3.186	[CIII] λ 1909
6846	53.1845741	-27.7833309	25.193	7990.1 ± 24.4	16	1.144	[OII] λ 3727
6853	53.1518402	-27.7828617	23.428	6964.1 ± 26.3	24	0.869	[OII] λ 3727
				9280.7 ± 36.9	55	0.858	[OIII] $\lambda\lambda$ 4959,5007
6893	53.1927605	-27.7835293	25.334	7180.5 ± 41.1	28	0.438	[OIII] $\lambda\lambda$ 4959,5007
6953	53.1527824	-27.7826958	24.721	6609.8 ± 37.5	10	0.774	[OII] λ 3727
				8812.3 ± 41.0	53	0.764	[OIII] $\lambda\lambda$ 4959,5007
6959	53.1765175	-27.7825508	25.051	6636.4 ± 21.3	38	0.329	[OIII] $\lambda\lambda$ 4959,5007
				8784.3 ± 25.3	21	0.338	H α
7131	53.1352577	-27.7816753	24.314	9121.6 ± 33.3	8	1.447	[OII] λ 3727
7398	53.1763268	-27.7808590	24.892	7576.1 ± 27.2	50	0.517	[OIII] $\lambda\lambda$ 4959,5007
7687	53.1505852	-27.7712173	23.030	6284.6 ± 9.1	23	0.258	[OIII] $\lambda\lambda$ 4959,5007
				8155.5 ± 35.3	64	0.243	H α

Table 1—Continued

UDF ID	RA	DEC	i-mag (AB)	Wavelength ^a Å	Measured Line Flux ^b $10^{-18} \text{ erg/s/cm}^2$	Redshift	Line
7847	53.1739960	-27.7720566	21.227	8821.8 ± 71.6	231	0.344	H α
7889	53.1844864	-27.7722511	25.113	9221.3 ± 37.3	21	0.846	[OIII] $\lambda\lambda$ 4959,5007
8026	53.1512146	-27.7728405	23.967	7912.0 ± 24.5	71	0.206	H α
8040 ^d	53.1619606	-27.7739010	22.532	6359.6 ± 38.2	43	0.273	[OIII] $\lambda\lambda$ 4959,5007
				8388.3 ± 41.8	29	0.278	H α
8040 ^d	53.1619606	-27.7739010		6308.2 ± 28.0	59	0.263	[OIII] $\lambda\lambda$ 4959,5007
				8367.8 ± 56.9	39	0.275	H α
8157 [†]	53.1649513	-27.7736721	28.344	6407.1 ± 5.5	6	0.000	
8680	53.1477776	-27.7769489	23.995	7780.0 ± 21.4	4	1.087	[OII] λ 3727
8744	53.1466179	-27.7774906	25.416	7819.3 ± 27.1	5	0.191	H α
9040	53.1711852	-27.7784585	26.183	7350.9 ± 50.1	13	5.045	Ly α
9088	53.1463623	-27.7700825	25.281	7891.7 ± 27.1	7	0.580	[OIII] $\lambda\lambda$ 4959,5007
9244	53.1615181	-27.7676182	23.685	8380.4 ± 31.1	41	0.678	[OIII] $\lambda\lambda$ 4959,5007
9340	53.1694679	-27.7655869	27.517	6940.5 ± 23.7	15	4.708	Ly α
9397 ^e	53.1628532	-27.7671661	21.020	6225.0 ± 34.4	747	1.225	[MgII] λ 2798
				7080.8 ± 29.9	140		FeII complex
				9661.6 ± 35.9	69		H γ -FeII-[OIII] complex
9437	53.1492195	-27.7637062	23.483	8684.1 ± 54.8	32	0.323	H α
9487	53.1673927	-27.7668190	27.204	6194.0 ± 30.7	17	4.094	Ly α
9712	53.1579247	-27.7552757	25.514	7142.5 ± 48.5	17	0.916	[OII] λ 3727
				9533.8 ± 68.4	15	0.909	[OIII] $\lambda\lambda$ 4959,5007
9765	53.1516647	-27.7613010	23.581	7448.4 ± 27.8	26	0.998	[OII] λ 3727
9962	53.1562233	-27.7573833	24.177	9196.2 ± 34.2	20	0.841	[OIII] $\lambda\lambda$ 4959,5007
10025	53.1704445	-27.7613754	21.517	7641.0 ± 37.8	131	0.164	H α

Table 1—Continued

UDF ID	RA	DEC	i-mag (AB)	Wavelength ^a Å	Measured Line Flux ^b $10^{-18} \text{ erg/s/cm}^2$	Redshift	Line
20037	53.1593552	-27.7750263	24.665	8273.6 ± 31.8	17	1.220	[OII] λ 3727
20039 [†]	53.1604271	-27.7752285	26.154	9168.0 ± 4.1	54	-1.000	
20061	53.1624680	-27.7803574	26.029	8586.0 ± 32.9	44	0.719	[OIII] $\lambda\lambda$ 4959,5007
20083	53.1865730	-27.7902279	23.658	7333.6 ± 19.2	74	0.468	[OIII] $\lambda\lambda$ 4959,5007

^aWavelength errors are the formal uncertainty from a gaussian fit to the line. Based on comparison of GRAPES redshifts with VLT redshifts (see text), we estimate that a systematic error floor of $\sim 12\text{\AA}$ should be applied when the quoted error is smaller.

^bFluxes quoted here are directly measured from the emission features falling within the grism extraction window. Because this window is often relatively narrow, we estimate that the total emission line flux of an object could exceed the tabulated fluxes by aperture correction factors in the range of ~ 1.5 to ~ 3 .

[†]These objects are manually added into the emission line list.

^cine flux and redshift for object 5225 are taken from Rhoads et al 2005.

^dObject 8040 in the UDF catalog corresponds to two distinct catalog entries in an earlier GRAPES catalog, which likely correspond to a pair of HII regions in the same galaxy. The two regions were analyzed separately by “emlinecull,” resulting in two table entries for this object. The total line flux for the object is approximately the sum of the two entries, while both have the same redshift within the uncertainties.

^eine identifications for object 9397 are based on comparison with the composite quasar spectra of Francis et al (1991) and vanden Berk et al (2001). The redshift is based on the MgII line.

Table 2. Redshift comparison between GRAPES and ground-based spectra.

UDF	z (GRAPES)	z (VLT)	reference ^a
-100	0.601	0.218,0.6354 ^b	1,2
-101	0.138	0.132	2
-104	1.218	1.220	4
900	0.419	0.414	2,3
1000	0.232	0.213	2
1446	2.470	2.470	5
1752	1.238	1.244	1
2201	1.377	1.382	4
3484	0.405	0.947	2
4142	0.729	0.737	1
4396	1.218	1.223	1
4445	0.922	0.458	3
4816	1.230	1.220	1
4929	0.438	0.438	2,3
4981	1.430	1.438	4
5606	0.254	0.229	2
5620	0.226	0.212	2
6732	3.193	3.193	3
6953	0.764	0.765	4
7847	0.344	0.333	1,2
8680	1.088	1.086	4
9397	3.017	1.216	3
20037	1.220	1.215	4

^aThe references: (1) Vanzella et al. 2005; (2) Le Fevre et al. 2004; (3) Szokoly et al. 2004; (4) Vanzella et al. 2006; (5) Grazian et al. 2006

^bObject -100 has discrepant ground-based redshifts. The database of Le Fevre et al yields

$z = 0.6354$, in rough agreement with the GRAPES value, while the database of Vanzella et al (2005) gives 0.218.